

## Article

# Finite Element Analysis Study of Buried Crack Defects in B-Sleeve Fillet Welds

Hao Zhang <sup>1</sup>, Zhengxin Wei <sup>2</sup>, Xinzhan Li <sup>3</sup>, Zhanwei Yuan <sup>4,\*</sup> and Min Guo <sup>5,\*</sup><sup>1</sup> CNPC Tubular Goods Research Institute, Xi'an 710077, China<sup>2</sup> Lanzhou Gas Transmission Branch, National Pipeline Network Group, Lanzhou 730060, China<sup>3</sup> Gansu Shaanxi Gas Transmission Branch, West East Gas Transmission Company of State Grid Corporation of China, Lanzhou 730030, China<sup>4</sup> School of Materials Science and Engineering, Chang'an University, Xi'an 710064, China<sup>5</sup> Inner Mongolia Metal Material Research Institute, Baotou 014010, China

\* Correspondence: yuanzhw@chd.edu.cn (Z.Y.); guomin-2014@sohu.com (M.G.)

**Abstract:** Since it is difficult to study the influence of different defect characteristics on the stress intensity factor of B-type sleeve fillet welds via experiments, this paper adopts ABAQUS finite element analysis software (Version 2019) to model the B-type sleeve fillet welds and studies the stress and stress intensity factor under different crack lengths, heights, and angles. The simulation results showed that with the increase in crack length and depth, the maximum stress intensity factor gradually increased, and with the increase in the crack inclination angle, the maximum stress intensity factor first increased and then decreased.

**Keywords:** stress intensity factor; finite element simulation; cracks; fillet welds



**Citation:** Zhang, H.; Wei, Z.; Li, X.; Yuan, Z.; Guo, M. Finite Element Analysis Study of Buried Crack Defects in B-Sleeve Fillet Welds. *Coatings* **2024**, *14*, 560. <https://doi.org/10.3390/coatings14050560>

Academic Editors: Giorgos Skordaris, Alexander S. Lenshin and Vladimir Kashkarov

Received: 12 March 2024

Revised: 26 April 2024

Accepted: 28 April 2024

Published: 1 May 2024



**Copyright:** © 2024 by the authors. Licensee MDPI, Basel, Switzerland. This article is an open access article distributed under the terms and conditions of the Creative Commons Attribution (CC BY) license (<https://creativecommons.org/licenses/by/4.0/>).

## 1. Introduction

Since the 20th century, there has been a consistent rise in global oil demand, accompanied by an annual increase in the number of oil pipeline projects worldwide. At present, China's pipeline projects are characterized by long pipeline distances, wide coverage, and susceptibility to environmental influences [1,2], and about 70% of China's pipelines have been in use for decades, exceeding their original expected lifespan [3,4]. The aging and corrosion of pipelines have seriously restricted the transportation safety of oil and gas pipelines in China [5]. Addressing pipeline aging and corrosion, two predominant repair strategies have emerged: traditional methods and in-service welding techniques. Traditional repair methods necessitate ceasing pipeline transportation and pressure, actions that can lead to both environmental pollution and economic losses. As an effective in-service welding repair method, B-sleeve repair technology can effectively overcome these two problems, so it is gradually becoming the main repair method [6–9].

In the implementation of B-sleeve repair technology, a large number of annular fillet welds need to be used to weld the sleeve to the pipe [10], and in the process of welding, the annular fillet weld area often produces porosity, slag, and other defects. The existence of these defects will affect the quality of the repair, become a source of cracks, and even produce leakage potential [11,12]. Fillet welds, located at structural discontinuities, are prone to stress corrosion cracking at lower stress levels, presenting a linear elastic fracture mechanics issue. Liu [13], through numerical simulations and experiments, found that the peak value of the defective echo signals obtained from phased-array ultrasonic fan scanning was positively correlated with the diameter of pore defects, which provides a reliable means of quantitative analysis of the pore defects. In the extreme case of complete cracking of the pipe ring weld, the ultimate bending moment that can be withstood by the B-sleeve fillet weld is about 69% of that of the pipe base material [14]. The stress intensity factor is an important parameter to control the linear elastic fracture, and there are many

ways to calculate it, including analytical methods, finite element analysis, simulated crack extension, crack virtual closure techniques, J-integral analysis, nodal methods, boundary element analysis, and weight function methods. Although the analytical method can obtain high accuracy, it is not always applicable in practical engineering due to the complexity of crack-containing structures, different crack morphologies, and different loading conditions. In contrast, finite element analysis transcends the limitations of structural complexity and crack geometry, delivering the requisite accuracy for practical engineering applications [15]. Yuan [16] used the J-integral method, pushover method, and interaction integral method to simulate the K-value, and the results showed that the K-value of the crack tip of the fracture model was in good agreement with the K-value of the crack tip calculated by the three different methods. M. Gintalas et al. [17] provided a normalized T-stress solution for through-wall cracked tubes under bending, based on a series of finite element calculations that are applicable to all kinds of crack sizes and pipe radius to wall thickness ratios. Behzad V. Farahani [18] used advanced discretization techniques, the radial point interpolation meshless method, and the finite element method to obtain stress distributions and calculate stress intensity factor ranges. Yu H et al. [19] investigated the safety performance of cracked annular welds in in-service pressure vessels based on fracture mechanics and calculated the crack tip stress intensity factor by using joint simulation with ABAQUS. The effects of crack location, length, and depth on the crack tip stress intensity factor were analyzed. M. Iqbal et al. [20] explored a tubular KT joint with semi-elliptical cracks under axial tensile loading. The fracture tool of ANSYS Structural was utilized to simulate the joint, and the effects of crack size, location, and fiber-reinforced polymer reinforcement on the stress intensity factor were evaluated. S. Shahrooi et al. [21] proposed a new strategy for the two-dimensional problem, which included an extended isometric analysis method for detecting the cracking behavior of pipeline structures. Non-rational B-spline homogeneous functions were used to approximate the solution field, taking into account its geometric constraints.

As a result, the finite element method has become a common means of calculating stress intensity factors. In this study, based on the finite element analysis calculations of a preset elliptical crack at the location of the fillet weld, the influence of parameters, such as the geometry of the built-in defect, its location in the fillet weld, and the casing characteristics on the stress intensity factor, was analyzed. The stress intensity factor data at the crack tip location under the internal pressure load of the pipe were calculated, and a theoretical model was established based on the obtained stress intensity factor data, as well as parameters such as pipe structure and crack characteristics, which provides a basis for the safe use of cracked fillet-welded pipes.

## 2. Finite Element Modeling

### 2.1. Geometry Modeling

In this study, the diameter of the pipe was 1219 mm, and the wall thickness was 18.4 mm, ensconced within a casing of 28.5 mm thickness. Since the pipe model is an axisymmetric model, the simulation was carried out using the 1/2 model in order to improve the computational efficiency. In addition, in order to eliminate the marginal effect, the length from the fillet weld to the end was 3000 mm, the interval between the casing and the pipe was 3 mm, and the fillet weld area was an isosceles right triangle, as shown in Figure 1.

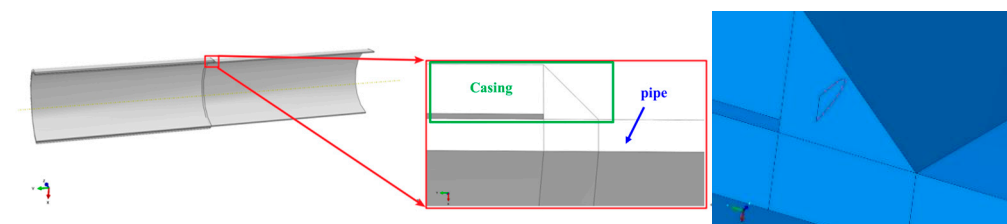


Figure 1. Pipe geometry model and cracks in the fillet welds.

## 2.2. Material Properties

The pipe, weld, and casing locations have different material properties, mainly elastic parameters, including modulus of elasticity and Poisson's ratio. The model material properties are shown in Table 1.

**Table 1.** Model material properties.

Component	Young's Modulus/GPa	Poisson's Ratio
plumbing	206	0.33
trocar	206	0.33
weld	215	0.33

## 2.3. Boundary Conditions and Loads

In order to emulate the actual working conditions, the model incorporated fixed constraints at both ends, axisymmetric constraints in the Y direction for the pipe cross-section, and an outward internal pressure of 10 MPa applied to the inner wall of the pipeline, as depicted in Figure 2.

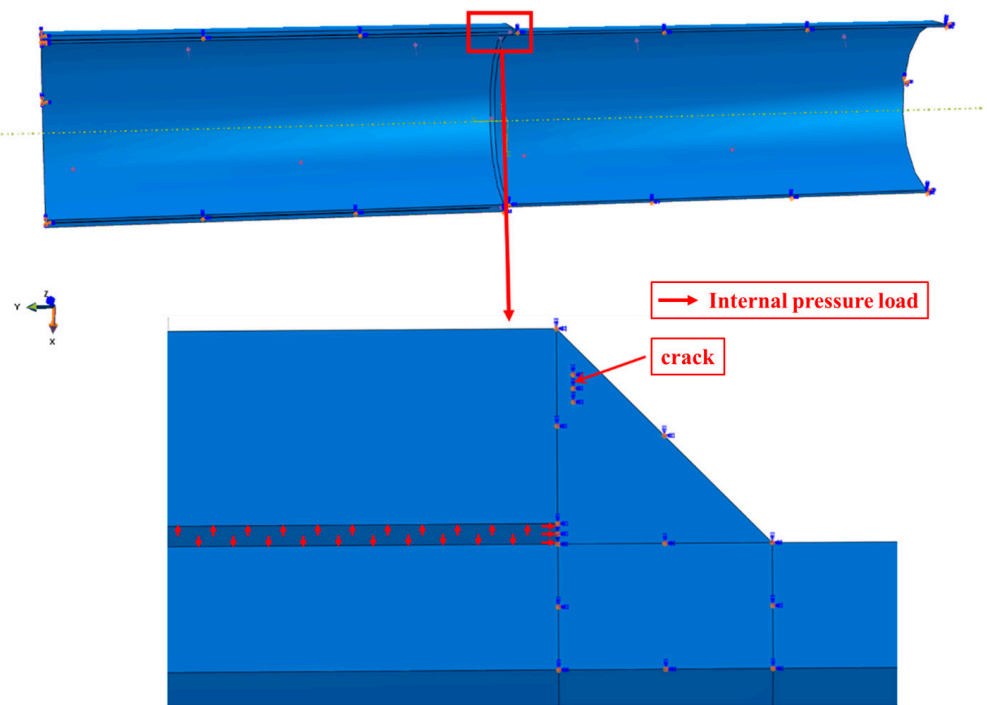


**Figure 2.** Boundary condition settings of the model.

In the study, the fillet weld region was divided into different blocks to investigate the effects of cracks at different locations on the stress intensity factor, as shown in Figure 3. A right-angle coordinate system was established by using the two right-angled edges of the fillet weld as x- and y-axes, and the horizontal and vertical coordinates  $P_x$  and  $P_y$  were taken in the range of 0 to 25 mm. The cracks were elliptical in shape, and the L1–5 coordinates of different crack locations are also labeled in Figure 3.

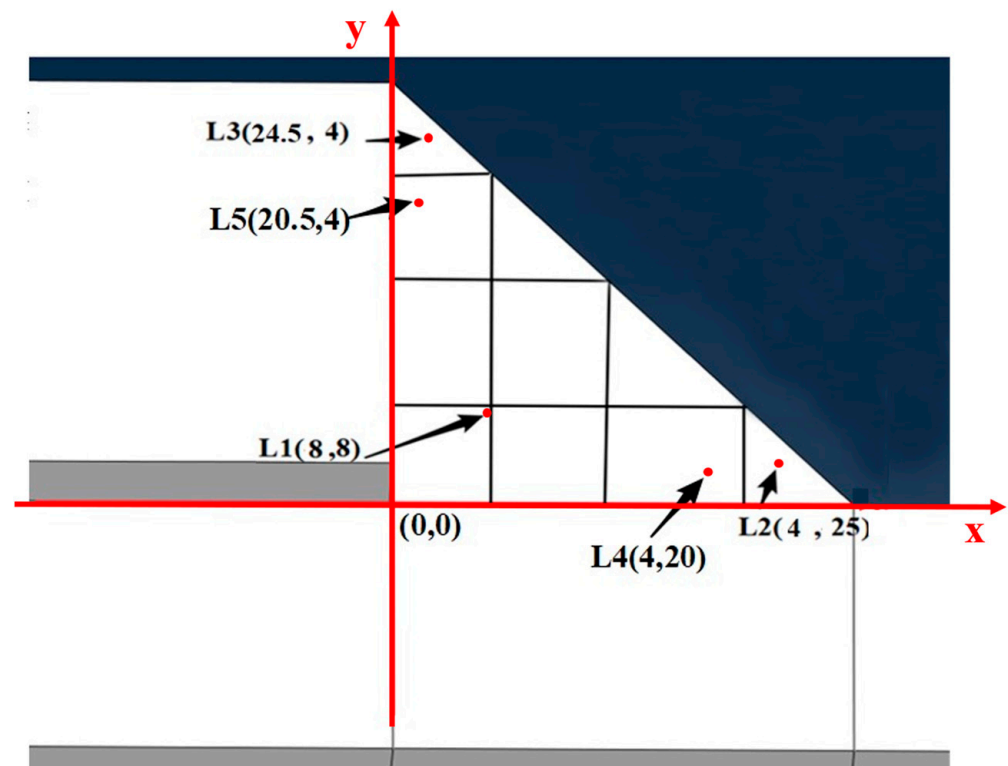


**Figure 3.** Schematic location of crack centers at the fillet weld position.

Upon commencement of the modeling calculations, the model was denoted as LX-XvXvX°, with 'L1-30v3v45°'; for instance, indicating a crack located at the L1 position with a length of 30 mm, a height of 3 mm, and an angle of 45°.

### 3. Results and Analysis

#### 3.1. Grid Size Effects

In order to determine the influence of the mesh size on the simulation results during the simulation process, the inserted cracks were divided into mesh sizes of 0.25 mm, 0.2 mm, 0.15 mm, 0.1 mm, and 0.05 mm, with the mesh size of 0.25 mm, 0.15 mm, 0.1 mm, and 0.05 mm, respectively, as shown in Figure 4a–e, for example, in the case of L1-10v3. The calculated maximum stress intensity factors are shown in Figure 4f, which were 48.51 MPa·m<sup>1/2</sup> for a grid size of 0.05 mm, 48.45 MPa·m<sup>1/2</sup> for a grid size of 0.1 mm, 48.41 MPa·m<sup>1/2</sup> for a grid size of 0.15 mm, and 48.41 MPa·m<sup>1/2</sup> for a grid size of 0.2 mm. The maximum stress intensity factor was 48.39 MPa·m<sup>1/2</sup> for a mesh size of 0.2 mm and 48.2 MPa·m<sup>1/2</sup> for a mesh size of 0.25 mm. The smaller the mesh size, the larger the maximum stress intensity factor, the higher the simulation accuracy, but the longer the simulation calculation time. In order to ensure the accuracy of the calculation results and improve the calculation efficiency, the mesh size of the model was chosen as 0.15 mm.

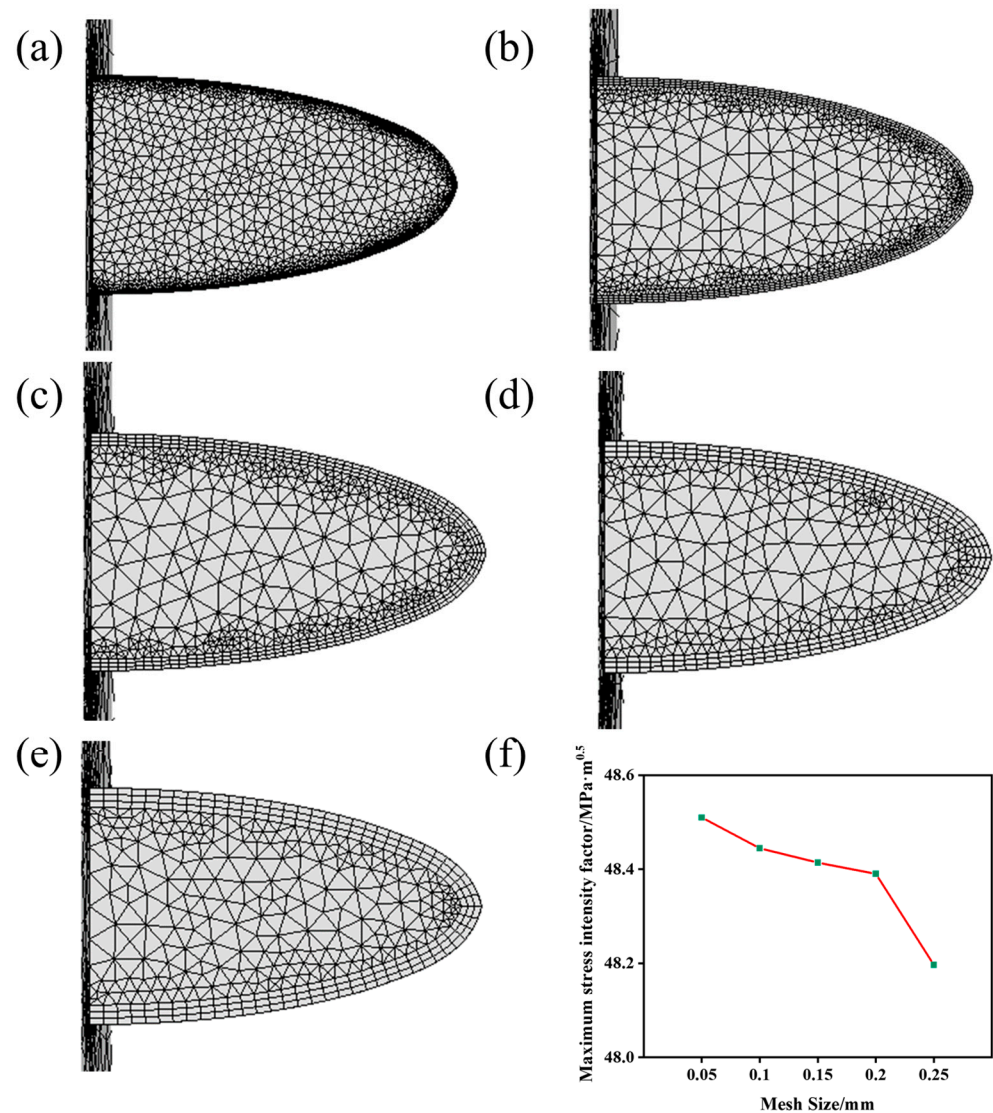


**Figure 4.** Different mesh sizes for L1-10v3: (a) 0.05 mm mesh, (b) 0.1 mm mesh, (c) 0.15 mm mesh, (d) 0.2 mm mesh, and (e) 0.25 mm mesh. (f) Maximum stress intensity factor calculation results.

### 3.2. Effect of Crack Length

L1-10v3 was taken as an example to analyze the stress distribution and the change in stress intensity factor at the crack location. The fillet weld crack was planned, and Figure 5 shows the stress distribution after bearing the buried crack L1-10v3, where maximum (Max.) principal, middle (Mid.) principal, and minimum (Min.) principal are the principal stresses in different directions. From the figure, it can be seen that the stresses inside the elliptical crack region were obviously slightly higher than the stresses outside the region, but no obvious stress concentration was found. From the results of different principal stresses, it can be found that the different principal stresses were higher in the region around the tip of the crack line, with the maximum stress reaching 596.1 MPa, and these locations are the regions where the crack extended further outward. Figure 6 shows the variation of the stress intensity factor at different locations on the L1-10v3 crack, where the horizontal coordinates are the results of the normalization of the crack location, in which the stress intensity factor at location A was the largest,  $48.41 \text{ MPa}\cdot\text{m}^{1/2}$ , and that at the crack tip location was the smallest,  $24.15 \text{ MPa}\cdot\text{m}^{1/2}$ , which may be due to the small curvature at locations A and B, and close-to-the-crack-tip location of the curvature was large.

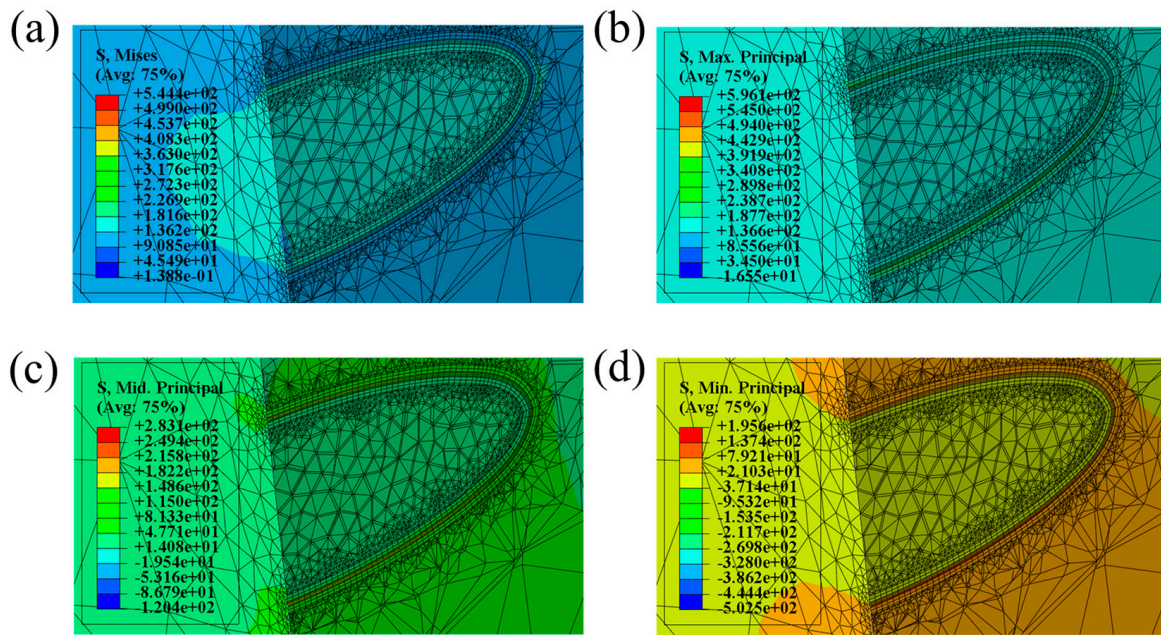


Figure 5. Stress distribution at the crack location of L1-10v3: (a) Mises stress, (b) first principal stress, (c) second principal stress, and (d) third principal stress.

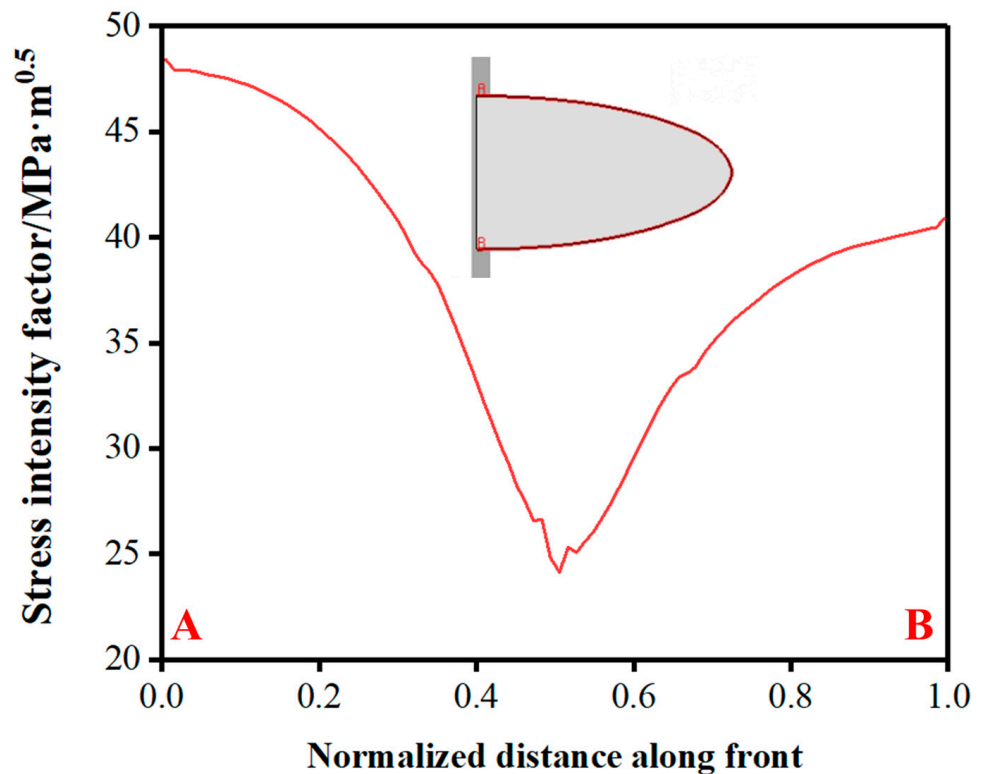


Figure 6. Calculated results of the L1-10v3 stress intensity factor.

To systematically assess the impact of the buried crack’s length on the stress intensity factor, we conducted comparative analyses, simulating the maximum stress intensity factor under load for cracks of varying lengths, with the crack depth fixed at 3 mm and the crack positioned at L1. Simulation results, as depicted in Figure 7, revealed that for a crack length of 10 mm, the maximum stress intensity factor was 48.6 MPa·m<sup>1/2</sup>. This value escalated with an increase in the crack length, reaching a maximum stress intensity factor

of  $52.25 \text{ MPa}\cdot\text{m}^{1/2}$  for a 50 mm crack length. The relationship between the maximum stress intensity factor and the lengths of the three cracks examined suggested a near-linear increase. A regression analysis of the maximum stress intensity factor for different crack lengths, considering a crack height of 3 mm at the L1 position, yielded the fitted equation presented in Equation (1):

$$K = 46.48 + 0.26L - 0.0028L^2 \tag{1}$$

where K is the maximum stress intensity factor and L is the crack length.

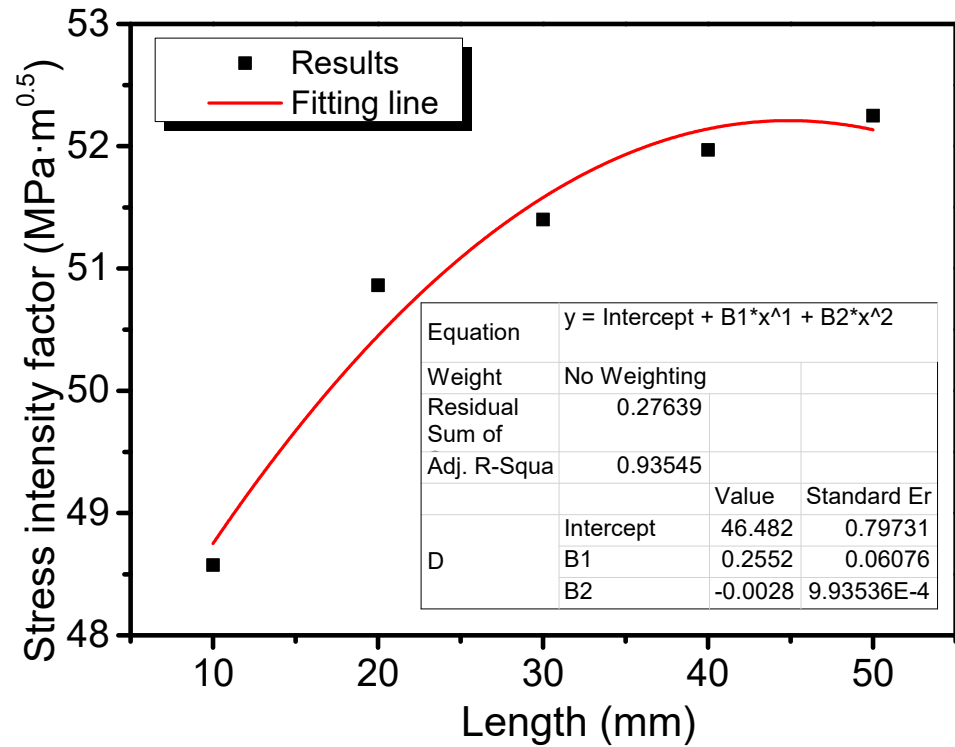


Figure 7. Comparison of maximum stress intensity factors for different crack lengths at the same location.

### 3.3. Effect of Crack Depth

The maximum stress intensity factor after loading with different crack heights at the L position is shown in Figure 8. From the figure, it can be seen that the maximum stress intensity factor was  $52.4 \text{ MPa}\cdot\text{m}^{1/2}$  when the height of the crack itself was 3 mm. With the increase in the height of the crack itself, the maximum stress intensity factor was increasing, and the maximum stress intensity factor was  $105.76 \text{ MPa}\cdot\text{m}^{1/2}$  when the height of the crack itself was 8 mm. The maximum stress intensity factor under the different heights of the crack itself increased approximately linearly, and the maximum stress intensity factor under different heights of the crack itself at position L was fitted. At a length of 30 mm, the maximum stress intensity factor under different heights of the crack itself was fitted, and the fitted equation is shown in Equation (2):

$$K = 29.04 + 6.88w + 0.34w^2 \tag{2}$$

where K is the maximum stress intensity factor and w is the height of the crack itself.

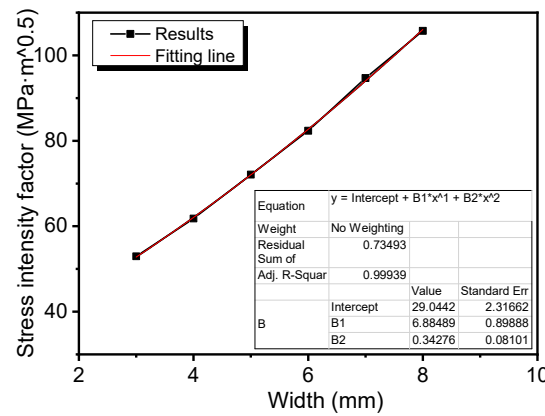


Figure 8. Comparison of maximum stress intensity factors at the same location with different heights of the crack itself.

### 3.4. Crack Angle Effects

The maximum stress intensity factor after bearing at different crack angles in the L position is shown in Figure 9a. From the figure, it can be seen that the results of the maximum stress intensity factor at different angles differed greatly: the stress intensity factor at 30° was 67.44 MPa·m<sup>1/2</sup>, and the stress intensity factor at the 90° position was the largest, which was 102.4 MPa·m<sup>1/2</sup>. The maximum stress intensity factor at 120° was 60.9 MPa·m<sup>1/2</sup>, and the result is close to that of the maximum stress intensity factor at 30°. It can be found that the value of the maximum stress intensity factor increased with the increase of the crack angle from 0 to 90°, and the stress intensity factor was at its maximum when the crack angle was 90°. At a crack angle of 90~180°, the maximum stress intensity factor value started to decrease with the increase in the crack angle. The normalized results of the maximum stress intensity factor at different crack angles are shown in Figure 9b, and the fitted equation is shown in Equation (3):

$$K = 0.9958 + 0.055\sin(\theta) + 0.886\sin^2(\theta) \tag{3}$$

where K is the maximum stress intensity factor and  $\theta$  is the crack angle.

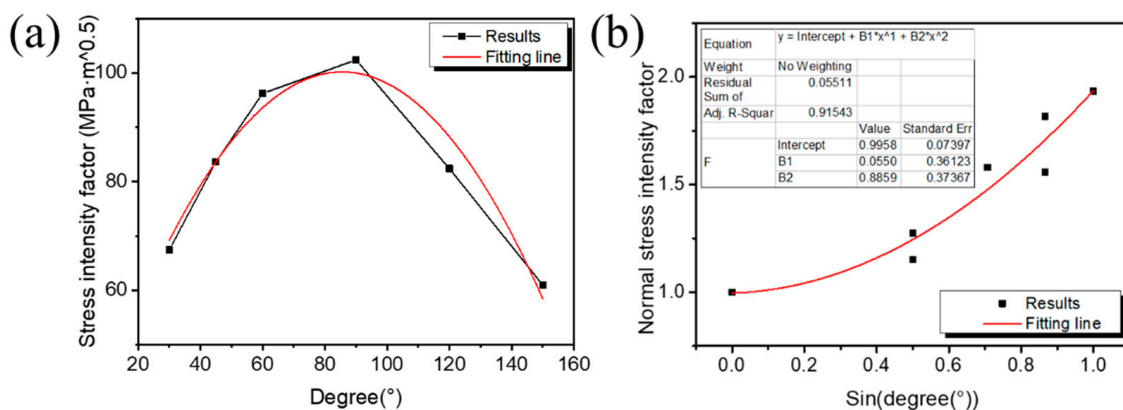


Figure 9. (a) Maximum stress intensity factor results for different crack angles. (b) Maximum stress intensity factor normalized results.

### 3.5. Effect of Crack Location

The simulation results of the maximum stress intensity factor under the same crack geometry at different locations under L position are shown in Figure 10a. From the figure, it can be seen that the results of the maximum stress intensity factor under different positions were very different: the stress intensity factor at L1 position was 51.4 MPa·m<sup>1/2</sup>, and the

stress intensity factor at L2 position was the largest, which was  $143.7 \text{ MPa}\cdot\text{m}^{1/2}$ . The reason for analyzing the results is mainly due to the fact that the crack was close to the edge of the fillet weld in this position, and the stress was more concentrated. The results of the L3 and L5 positions were similar to those of the maximum stress intensity factor of the L1 position. The results at L3 and L5 were close to the maximum stress intensity factor at L1. It can be found that the closer the crack is to the outer edge of the fillet weld, the larger the value of the maximum stress intensity factor. The normalized results of the maximum stress intensity factor at different crack positions are shown in Figure 10b, and the fitted equations are shown in Equations (4) and (5):

$$K = 139.75P + 10.50 \tag{4}$$

$$P = ((Px - 0.62)^2 + (Py - 0.24)^2)^{0.5} \tag{5}$$

where K is the maximum stress intensity factor, Px is the normalized coordinate of the horizontal coordinate position, and Py is the normalized coordinate of the vertical coordinate position, which indicates the relative position of the longitudinal coordinate of the crack in the coordinates of the fillet weld.

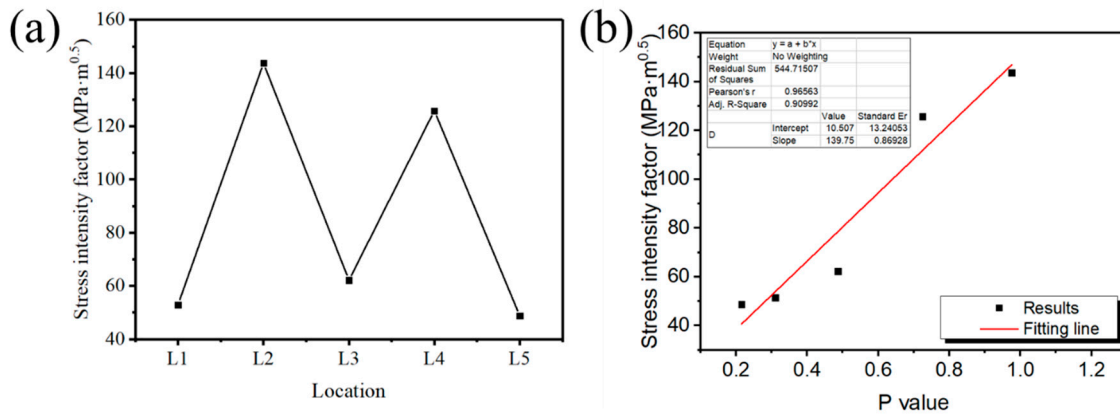


**Figure 10.** (a) Maximum stress intensity factor results for different crack locations. (b) Maximum stress intensity factor normalized results.

Considering the crack length, its own height, angle, and position, regression was performed to obtain the L position statistical model, and the maximum stress intensity factor prediction formula was obtained, as shown in Equation (6):

$$K = 0.0003508 * (46.48 + 0.26L - 0.0028L^2) * (29.04 + 6.88w + 0.34w^2) * (0.9958 + 0.055\sin(\theta) + 0.886\sin^2(\theta)) * (139.75P + 10.50) \tag{6}$$

where K is the maximum stress intensity factor, L is the length of the crack, w is the height of the crack itself, P is the crack position, and  $\theta$  is the crack angle.

The prediction error calculation formula is shown in Equation (7):

$$Errors = \frac{KIC_{prediction} - KIC_{simulation}}{KIC_{simulation}} \tag{7}$$

where KIC represents the maximum stress intensity factor at the crack tip.

Figure 11 displays a comparison of the predictive outcomes against the simulation results for the L position, with the red dots representing the predicted data points. An analysis of both the simulation and prediction results, facilitated by an error formula, was conducted. The findings indicated a strong concurrence between the predictions and the simulations, with the maximum error in predictions being confined to a 25% margin.

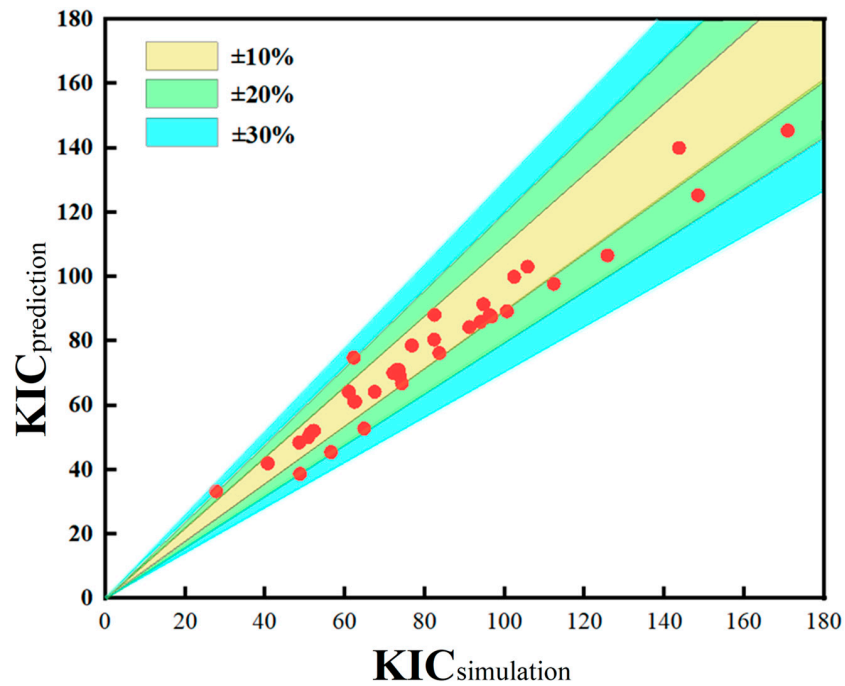


Figure 11. Error in prediction results.

Sy/t6477 is a residual strength evaluation method for oil and gas pipelines containing defects. The results of the stress intensity factor predicted by Sy/t6477 are shown in Figure 12, which were compared with the simulation results and showed a positive correlation. SIF stands for stress intensity factor. The fitting equation is shown in Equation (8):

$$K = 159.59 - 7.14s + 0.117s^2 \tag{8}$$

where  $K$  is the maximum stress intensity factor and  $s$  is the stress intensity factor calculated by Sy/t6477. The formula for the maximum stress intensity factor predicted by Sy/t6477 after considering the crack angle and crack location is shown in Equation (9):

$$K = 0.01654 \times (159.59 - 7.14s + 0.117s^2) \times (0.9958 + 0.055\sin(\theta) + 0.886\sin^2(\theta)) \times (139.75P + 10.50). \tag{9}$$

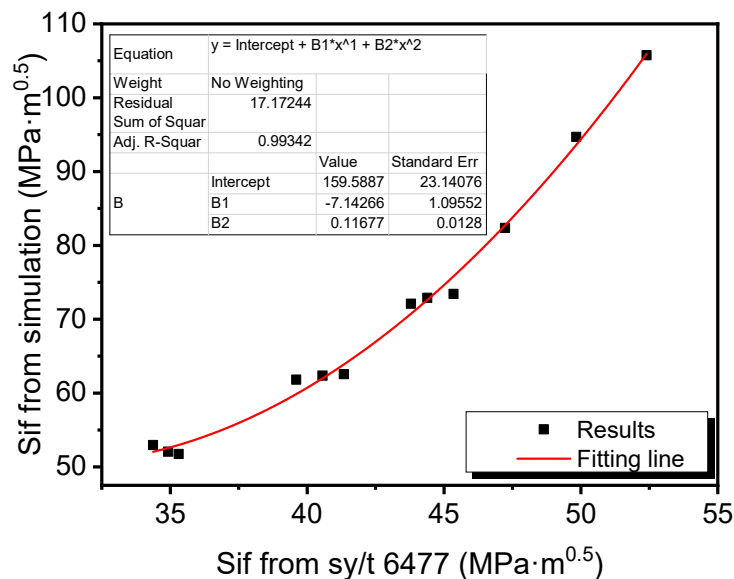


Figure 12. Relationship between stress intensity factors predicted by Sy/t6477 and simulation results.

Figure 13 shows a detailed comparison of the  $S_y/t6477$  predicted results with the simulated results at location L. The red data points in the figure indicate the predicted results. The simulated and  $S_y/t6477$ -predicted data were evaluated and analyzed in detail with the help of the error formula. The analysis results showed that the predictions were in good agreement with the simulations, with most of the prediction errors staying within the 30% threshold, with some exceptions at specific locations.

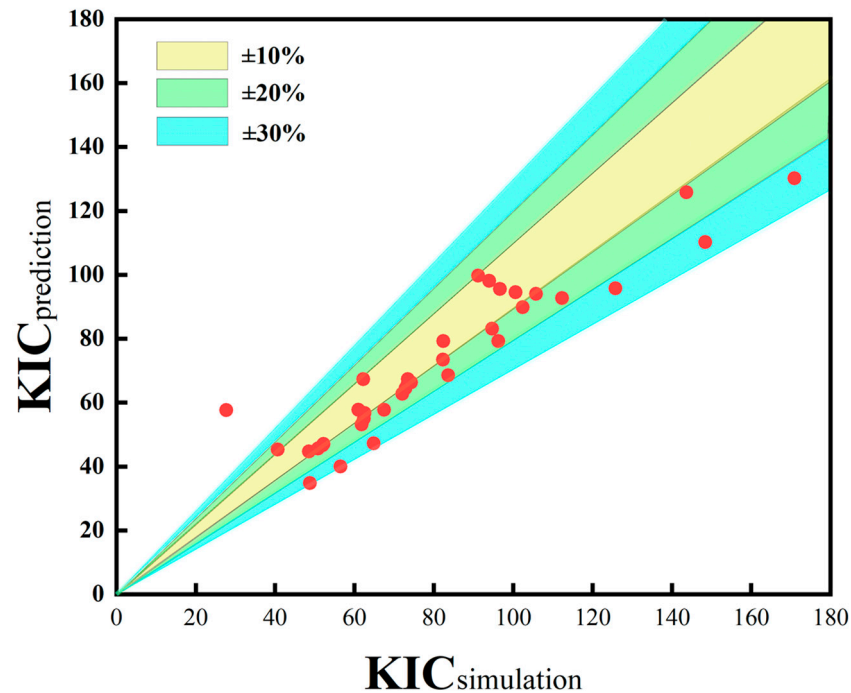


Figure 13.  $S_y/t6477$  prediction result errors.

#### 4. Conclusions

- (1) Different crack lengths at the same location had a significant effect on the maximum stress intensity factor. With the increase in length, the maximum stress intensity factor gradually increased, and within the parameter range of this study, the maximum stress intensity factor was linearly related to the crack length, with the equation:  $K = 46.48 + 0.26L - 0.0028L^2$ .
- (2) Different heights of the crack itself at the same position had obvious effects on the maximum stress intensity factor. With the increase of its own height, the maximum stress intensity factor gradually increased, and within the parameter range of this study, the maximum stress intensity factor was linearly related to the height of the crack itself, with the equation:  $K = 29.04 + 6.88w + 0.34w^2$ . From the influence law, it was found that the influence of length was relatively weak, and the influence of its own height was more significant.
- (3) As the crack inclination angle increased, the maximum stress intensity factor increased and then decreased, and the effect was greatest when the crack was parallel to the axial direction of the pipe and least when it was perpendicular.
- (4) A predictive model for the relationship between buried cracks and their characteristics was successfully formulated, with a maximum prediction error for buried cracks not exceeding 25%. This model provides a valuable tool for assessing the integrity of fillet weld pipes with embedded defects.
- (5)  $S_y/t6477$  was used to calculate the stress intensity factors and compare them with the simulation results, both of which showed a positive correlation, and to establish a prediction model. The maximum prediction error for buried cracks did not exceed 30%.

**Author Contributions:** Methodology, H.Z. and X.L.; Investigation, Z.W.; Data curation, Writing—original draft, Z.Y. and M.G. All authors have read and agreed to the published version of the manuscript.

**Funding:** This research received no external funding.

**Institutional Review Board Statement:** Not applicable.

**Informed Consent Statement:** Not applicable.

**Data Availability Statement:** Data are contained within the article.

**Conflicts of Interest:** Hao Zhang was employed by the company CNPC, Zhengxin Wei was employed by the company National Pipeline Network Group, Xinzhan Li was employed by the company West East Gas Transmission Company of State Grid Corporation of China while contributing to this manuscript, Our contributions to this work and manuscript were made independently without any requirement, guidance or input by my employer. We received no financial compensation from any source for the contributions made to this scientific work and manuscript. The remaining authors declare that the research was conducted in the absence of any commercial or financial relationships that could be construed as a potential conflict of interest.

## References

1. Sun, Y.; Lu, C. Analysis of thermal stress and influencing factors of gas pipeline based on finite element. *J. Xihua Univ. (Nat. Sci. Ed.)* **2018**, *37*, 19–22.
2. Yu, Z.; Zhang, W.; Zhang, Z.; Zhang, M.; Wang, C. Development direction of natural gas transmission pipeline and related technical issues in China. *Oil Gas Storage Transp.* **2012**, *31*, 321–325.
3. Zhang, B.; Qian, C.W.; Wang, Y.M.; Zhang, Y.Z. Development and application of high steel grade pipeline steel at home and abroad. *Pet. Eng. Constr.* **2012**, *38*, 1–4.
4. Li, D. Research status and development of oil and gas pipeline crack extension. *Henan Univ. Sci. Technol.* **2014**, *59*.
5. Sin, K.; Yang, F.; Wei, G.; Zhang, Z.; Yang, P.; Zheng, Y. Reflections on the design procedure and method of B-sleeve isotropic design for X80 class pipeline in service. *China Pet. Chem. Stand. Qual.* **2022**, *42*, 110–112.
6. Dong, S. Review of China's oil and gas pipeline integrity management in the past 20 years and development suggestions. *Oil Gas Storage Transp. Tion* **2020**, *39*, 241–261.
7. Zhao, X.; Wang, G.; Yang, F.; Bai, Q.; Liu, Y.; Xi, G.; Sun, B.; Nie, X.; Xu, Y. High-strength type-B sleeve for pipeline girth weld repair and its key application technology. *Oil Gas Storage Transp.* **2022**, *41*, 1141–1149.
8. Wang, G.; Ren, G.; Deng, B.; Zhang, L.; Jia, P. Verification Analysis of X70 Type B Sleeve for In-service Pipeline Repair. *J. Fail. Anal. Prev.* **2023**, *23*, 1137–1149. [[CrossRef](#)]
9. Li, R.; Zhang, W.; Yu, J.; Liu, S.; Zhao, Z.; Zhao, J.; Di, M. Interpretation of “Technical Specification for Defect Repair of Oil & Gas Pipeline”. *Pet. Eng. Constr.* **2020**, *46*, 88–92.
10. Lir, G.; Zhang, W.; Zhao, Z. Discussion on repair technology of girth weld defects of high-grade steel pipelines. *Oil Gas Storage Transp.* **2020**, *39*, 307–312.
11. Li, L.; Niu, X.; Liu, X.; Dai, G.; Chen, J.; Han, B. Current situation and prospect of ECA technology for high grade oil and gas pipelines. *Trans. Mater. Heat Treat.* **2021**, *42*, 20–28.
12. Huang, L.; Li, L.; Li, R.; Zhang, H.; Zhang, Y.; Liu, Y.; Yao, H.; Sun, S. Phased array ultrasonic inspection of B-sleeve lap welds. *Nondestruct. Test.* **2021**, *43*, 49–53.
13. Liu, Y.; Wu, Y.; Yang, F.; Tao, R.; Zhang, H.; Jia, P.; Pei, C.; Deng, G. Quantitative phased-array ultrasonic detection of defects in B-sleeve fillet welds. *Appl. Acoust.* **2023**, *42*, 145–153.
14. Cheng, Z.; Hu, C.; Duan, J.; Lv, Z.; Yang, T. Simulation experiment on mechanical properties of B-type sleeve fillet weld. *J. Southwest Pet. Univ.* **2021**, *43*, 111–118.
15. Liu, W.K.; Li, S.; Park, H.S. Eighty years of the finite element method: Birth, evolution, and future. *Arch. Comput. Methods Eng.* **2022**, *29*, 4431–4453. [[CrossRef](#)]
16. Yuan, H.; Li, J.; Xie, Y.; Hou, W. Computational analysis of crack tip stress intensity factor based on finite element method. *Mech. Manuf. Autom.* **2018**, *47*, 146–151.
17. Gintalas, M.; Ainsworth, R.A.; Scenini, F. T-stress solutions for through-wall circumferential cracks in straight pipes under bending. *Int. J. Press. Vessel. Pip.* **2017**, *152*, 27–37. [[CrossRef](#)]
18. Farahani, B.V.; Tavares, P.J.; Moreira PM, G.P.; Belinha, J. Stress intensity factor calculation through thermoelastic stress analysis, finite element and RPIM meshless method. *Eng. Fract. Mech.* **2017**, *183*, 66–78. [[CrossRef](#)]
19. Yu, H.; Li, J.; Zheng, N. Study on Stress Intensity Factor of Girth Weld with Crack Defects. *Acad. J. Sci. Technol.* **2024**, *9*, 119–122. [[CrossRef](#)]

20. Iqbal, M.; Karuppanan, S.; Perumal, V.; Ovinis, M.; Rasul, A. Numerical investigation of crack mitigation in tubular KT-joints using composite reinforcement. *Eng. Proc.* **2023**, *56*, 255. [[CrossRef](#)]
21. El Fakkoussi, S.; Moustabchir, H.; Elkhalfi, A.; Pruncu, C.I. Application of the Extended Isogeometric Analysis (X-IGA) to Evaluate a Pipeline Structure Containing an External Crack. *J. Eng.* **2018**, *2018*, 4125765. [[CrossRef](#)]

**Disclaimer/Publisher's Note:** The statements, opinions and data contained in all publications are solely those of the individual author(s) and contributor(s) and not of MDPI and/or the editor(s). MDPI and/or the editor(s) disclaim responsibility for any injury to people or property resulting from any ideas, methods, instructions or products referred to in the content.